

Model-independent test of gravity with a network of ground-based gravitational-wave detectors

Kazuhiro Hayama^{1,*} and Atsushi Nishizawa^{2,†}

¹*TAMA project, National Astronomical Observatory of Japan, Mitaka, Tokyo 181-8588, Japan,
Albert-Einstein-Institut (Max-Planck-Institut für Gravitationsphysik), Callinstraße 38, D-30167 Hannover, Germany*

²*Yukawa Institute for Theoretical Physics, Kyoto University, Kyoto 606-8502, Japan*

(Dated: August 23, 2012)

The observation of gravitational waves with a global network of interferometric detectors such as advanced LIGO, advanced Virgo, and KAGRA will make it possible to probe into the nature of space-time structure. Besides Einstein's general theory of relativity, there are several theories of gravitation that passed experimental tests so far. The gravitational-wave observation provides a new experimental test of alternative theories of gravity because a gravitational wave may have at most six independent modes of polarization, of which properties and number of modes are dependent on theories of gravity. This paper proposes a method to reconstruct the independent modes of polarization in time-series data of an advanced detector network. Since the method does not rely on any specific model, it gives model-independent test of alternative theories of gravity.

PACS numbers: 04.80.Cc, 04.30.-w, 04.80.Nn, 07.05.Kf

I. INTRODUCTION

In recent years, direct detection experiments of a gravitational wave (GW) have been well developed and the first generation of a kilometer-scale ground-based laser-interferometric GW detector has accomplished its design sensitivity. Although the first detection of the GW has not been achieved yet, the null detection has yielded scientific results [1–5]. The next-generation interferometers such as advanced LIGO [6], advanced VIRGO [7], and KAGRA [8] will be in operation in the coming five years and will bring valuable information about astronomical compact objects.

The direct observation of the GWs will also provide a unique opportunity to test the theory of general relativity (GR), through the propagation speed, waveforms, and polarization modes of GWs. In GR, a GW has two polarization modes (plus and cross modes), while in a general metric theory of gravitation, the GW is allowed to have at most six polarizations [9, 10]. In modified gravity theories such as the scalar-tensor theory [11, 12] and $f(R)$ gravity [13, 14], additional scalar polarizations appear (For more rigorous treatment of the polarizations with the Newman-Penrose formalism, see [15, 16]). On the other hand, in bimetric gravity theory [17] and massive gravity theory [18, 19], there appear at most six and five polarization modes, respectively, including scalar and vector modes [16, 20]. If the additional polarizations are found, it indicates that the theory of gravitation should be extended beyond GR and excludes some theoretical models, depending on which polarization modes are detected. Thus, the observation of the GW polarizations is a powerful tool to probe the extended law of gravity.

Currently, there are few observational constraints on the additional polarization modes of GWs. For the scalar GWs, the observed orbital-period derivative of PSR B1913+16 agrees well with predicted values of GR, conservatively, at a level of 1 % error [21], indicating that the contribution of scalar GWs to the energy loss is less than 1 %. However, it is important to cross-check the existence of the number of propagating degree of freedom directly by GW detection experiments, since these experiments probe in a weaker regime of gravity than a binary pulsar and at different distance scale. So far some authors have been proposed the method for separating a mixture of the polarization modes of the GW background and detecting non-Einsteinian polarization modes with pulsar timing array [22] and with ground-based laser-interferometric GW detectors [23, 24]. To decompose and reconstruct the polarization modes, the number of the independent signals of detectors should be more than that of polarization modes. In the above method with GW detectors, the number of polarizations are assumed to be three, since they considered a stochastic background.

Now we expect that more GW detectors will be in operation in the future, in total five detectors including two advanced LIGOs, advanced VIRGO, KAGRA, and IndIGO [25]. Then in principle we can reconstruct five polarization modes (all modes that GW detectors can separately detect) of a chirp and burst GW. In this paper, we propose a method to separate and reconstruct the polarization modes using observation data of multiple interferometric GW detectors. The proposed method does not need any theoretical waveform of the polarization modes of a GW, and therefore can be a model-independent probe of testing various alternative theories of gravity.

The organization of this paper is as follows. In section II we first describe antenna pattern functions of the tensorial and the scalar polarization modes, and then

*Electronic address: kazuhiro.hayama@ligo.org

†Electronic address: anishi@yukawa.kyoto-u.ac.jp

construct the algorithm to separate and reconstruct the polarization modes based on the coherent network analysis. In section IV A, we describe how the algorithm is implemented and show an example of reconstruction of the polarization modes. In section IV we made simulations of the reconstruction of the scalar polarization mode using simulated data of LIGO Hanford, LIGO Livingston, VIRGO, KAGRA. We devote the last section V to the summary of this paper.

II. ANALYTICAL METHOD OF RECONSTRUCTION

In this section, we provide the method separately detecting and reconstructing more than three polarization modes of a GW, which often appear alternative theories of gravity, with a coherent network of ground-based detectors.

A. Polarization modes of a gravitational wave

In general, a metric gravity theory in four dimensions allows at most six polarization modes of a GW [9, 10]. Let us define a wave orthonormal coordinate that are constructed by a unit vector \hat{k} directed to the propagation direction of a GW and two unit vectors \hat{e}_θ and \hat{e}_ϕ orthogonal to \hat{k} and each other. With these vectors, the polarization modes are defined as

$$\mathbf{e}^+ = \hat{e}_\theta \otimes \hat{e}_\theta - \hat{e}_\phi \otimes \hat{e}_\phi, \quad (1)$$

$$\mathbf{e}^\times = \hat{e}_\theta \otimes \hat{e}_\phi + \hat{e}_\phi \otimes \hat{e}_\theta, \quad (2)$$

$$\mathbf{e}^\circ = \hat{e}_\theta \otimes \hat{e}_\theta + \hat{e}_\phi \otimes \hat{e}_\phi, \quad (3)$$

$$\mathbf{e}^\ell = \sqrt{2} \hat{k} \otimes \hat{k}, \quad (4)$$

$$\mathbf{e}^x = \hat{e}_\theta \otimes \hat{k} + \hat{k} \otimes \hat{e}_\theta, \quad (5)$$

$$\mathbf{e}^y = \hat{e}_\phi \otimes \hat{k} + \hat{k} \otimes \hat{e}_\phi, \quad (6)$$

where the symbol \otimes denotes a tensor product. The $+$, \times , \circ , ℓ , x , and y polarization modes are called plus, cross, breathing, longitudinal, vector-x, and vector-y modes, respectively. According to rotation symmetry around the propagation axis of the GW, the $+$ and \times modes are identified with tensor-type (spin-2) GWs, the x and y modes are vector-type (spin-1) GWs, and the \circ and ℓ modes are scalar-type (spin-0) GWs. For the more detailed introduction, see [23]. With the sky direction of a GW source $\hat{\Omega} = -\hat{k}$, then a GW with the six polarizations is expressed as

$$h_{ij}(t, \hat{\Omega}) = \sum_A h_A(t) e_{ij}^A(\hat{\Omega}), \quad (7)$$

where $A = +, \times, \circ, \ell, x, y$.

B. Antenna pattern functions of polarization modes

Antenna pattern functions of the scalar and vector modes have been derived in [23, 26, 27]. We briefly summarize the results here.

Suppose m interferometric GW detectors are in operation. The GW signal of the I -th detector is written as

$$\xi_I(t, \hat{\Omega}) = \sum_A F_I^A(\hat{\Omega}) h_A(t), \quad (8)$$

where $F_I^A(\hat{\Omega})$ is the antenna pattern function of the I -th detector defined as

$$F_I^A(\hat{\Omega}) = e_{ij}^A(\hat{\Omega}) d_I^{ij}. \quad (9)$$

Here, d_I is a detector tensor defined as

$$d_I := \frac{1}{2} [\hat{u}_I \otimes \hat{u}_I - \hat{v}_I \otimes \hat{v}_I], \quad (10)$$

where \hat{u}_I, \hat{v}_I are unit vectors along with arms of the I -th detector. In a spherical coordinate (θ_I, ϕ_I) fixed to the I -th detector, since the detector coordinate $(\hat{u}, \hat{v}, \hat{w})$ and the wave coordinate $(\hat{e}_\theta, \hat{e}_\phi, \hat{\Omega})$ are related by

$$\hat{e}_\theta = \hat{u}_I \cos \theta_I \cos \phi_I + \hat{v}_I \cos \theta_I \sin \phi_I - \hat{w}_I \sin \theta_I, \quad (11)$$

$$\hat{e}_\phi = -\hat{u}_I \sin \phi_I + \hat{v}_I \cos \phi_I, \quad (12)$$

$$\hat{\Omega} = \hat{u}_I \sin \theta_I \cos \phi_I + \hat{v}_I \sin \theta_I \sin \phi_I + \hat{w}_I \cos \theta_I, \quad (13)$$

the angular pattern functions for each polarization are

$$F_I^+(\hat{\Omega}) = \frac{1}{2} (1 + \cos^2 \theta_I) \cos 2\phi_I, \quad (14)$$

$$F_I^\times(\hat{\Omega}) = -\cos \theta_I \sin 2\phi_I, \quad (15)$$

$$F_I^\circ(\hat{\Omega}) = -\frac{1}{2} \sin^2 \theta_I \cos 2\phi_I, \quad (16)$$

$$F_I^\ell(\hat{\Omega}) = \frac{1}{\sqrt{2}} \sin^2 \theta_I \cos 2\phi_I, \quad (17)$$

$$F_I^x(\hat{\Omega}) = -\frac{1}{2} \sin 2\theta_I \cos 2\phi_I, \quad (18)$$

$$F_I^y(\hat{\Omega}) = \sin \theta_I \sin 2\phi_I. \quad (19)$$

Note that the wave coordinate has a rotational degree of freedom ψ about the $\hat{\Omega}$ axis. The general formulas keeping ψ arbitrary are provided in [23]. From the expressions, one can see explicit rotational symmetries about ψ for the scalar, vector, and tensor polarization modes. In this paper we take $\psi = 0$ without loss of generality. Also we note that the above expressions are valid when the arm length of the detector, L , is much smaller than the wavelength of observed GWs, λ_g , i.e., $L \ll \lambda_g$. This condition is well satisfied for ground-based detectors we consider in this paper. The angular pattern functions for $L > \lambda_g$ have been derived in [28, 29] (For pulsar timing, see [30, 31]). Figure 1 shows the scalar, vector, and tensor antenna patterns as a function of the longitude and the latitude.

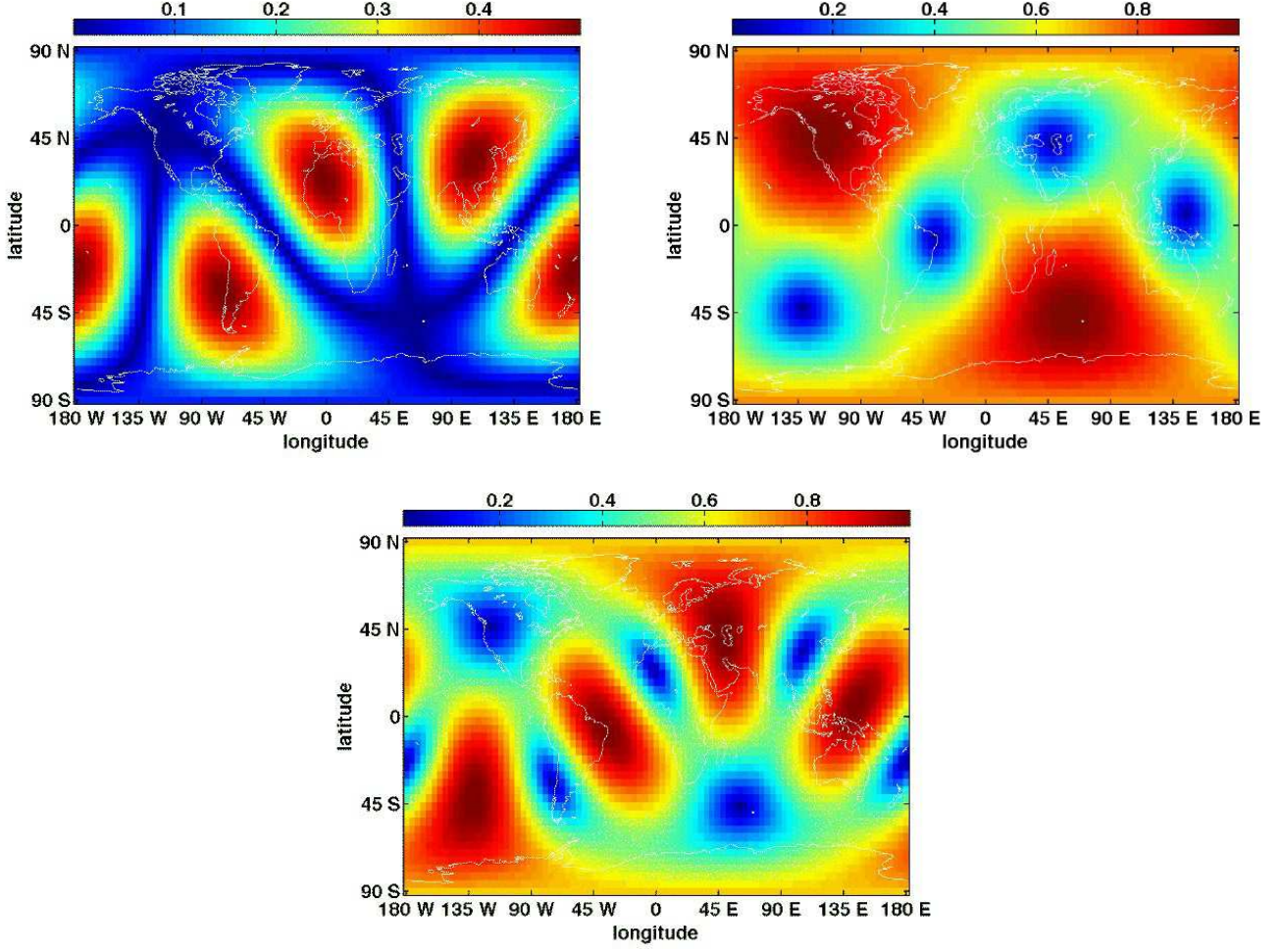


FIG. 1: The left top plot is an antenna pattern of LIGO interferometric detector at Hanford to a scalar GW $(F_o^2)^{1/2}$. The X-axis is the longitude and the Y-axis is the latitude. The right top plot is an antenna pattern function of the detector to the tensorial modes $(F_+^2 + F_\times^2)^{1/2}$. The bottom plot is an antenna pattern function of the detector to the vector modes $(F_x^2 + F_y^2)^{1/2}$.

The angular pattern functions for scalar modes in Eqs. (16) and (17) are degenerated. Thus, these GW signals of the scalar modes cannot be distinguished in GW observation and what we actually detect is the signal combination $\frac{1}{2}F_I^o\{h_o(t) - \sqrt{2}h_\ell(t)\}$. In addition, the scalar longitudinal mode often appears as a massive ghost mode in a modified gravity theory and should be removed from the theory. From these reasons, hereafter we assume that the longitudinal mode is absent. In addition, we assume that all polarization modes are massless since separate analysis is needed for the mode that propagates with the speed much different from that of light. Therefore, we consider in total five massless polarization modes (+, ×, ○, x, y) of a GW in the following sections.

C. Coherent network analysis

The coherent network analysis is an algorithm to find a GW signal in the data by combining all available detector data coherently ([32–37] and therein). The detector output is a combination of GWs in the polarization modes weighed by the pattern function of each polarization mode. In the coherent network analysis, the sky location of the GW and the waveforms in all polarization modes are reconstructed by inverting the set of the detector responses.

Data $x_I(t)$ from the I -th detector is

$$x_I(t) = \xi_I(t) + \eta_I(t), \quad (20)$$

where $\xi_I(t)$ and $\eta_I(t)$ are the GW signal and noise of the I -th detector. The noise is assumed to be Gaussian distributed. The arrival time of a GW at each detector is delayed depending on the geographical locations of the

GW detectors. If the relative time delay with respect to a reference time t_0 taken at the center of the Earth is defined as $\tau_I(\phi, \theta)$, the arrival time can be redefined as $t = t_0 + \tau_I(\phi, \theta)$.

All the detectors being taken into account, Eq. (20) is written as

$$\mathbf{x} = \mathbf{F}\mathbf{h} + \boldsymbol{\eta}, \quad (21)$$

where

$$\mathbf{x} = (\mathbf{x}_1, \dots, \mathbf{x}_m)^T, \quad (22)$$

$$\mathbf{F} = \begin{pmatrix} \mathbf{F}_1^+ & \mathbf{F}_1^\times & \mathbf{F}_1^\circ & \mathbf{F}_1^x & \mathbf{F}_1^y \\ \vdots & \vdots & \vdots & \vdots & \vdots \\ \mathbf{F}_m^+ & \mathbf{F}_m^\times & \mathbf{F}_m^\circ & \mathbf{F}_m^x & \mathbf{F}_m^y \end{pmatrix} \quad (23)$$

$$:= (\mathbf{F}_+, \mathbf{F}_\times, \mathbf{F}_\circ, \mathbf{F}_x, \mathbf{F}_y), \quad (23)$$

$$\mathbf{h} = (\mathbf{h}_+, \mathbf{h}_\times, \mathbf{h}_\circ, \mathbf{h}_x, \mathbf{h}_y)^T, \quad (24)$$

$$\boldsymbol{\eta} = (\boldsymbol{\eta}_1, \dots, \boldsymbol{\eta}_m)^T, \quad (25)$$

and

$$\mathbf{x}_I = (\hat{x}_I(f_0), \dots, \hat{x}_I(f_{N-1})), \quad (26)$$

$$\mathbf{F}_I^A = (\hat{F}_I^A(\hat{\Omega}, f_0), \dots, \hat{F}_I^A(\hat{\Omega}, f_{N-1}))^T, \quad (27)$$

$$\mathbf{h}_A = (\tilde{h}_A(f_0), \dots, \tilde{h}_A(f_{N-1})), \quad (28)$$

$$\boldsymbol{\eta}_I = (\hat{\eta}_I(f_0), \dots, \hat{\eta}_I(f_{N-1})). \quad (29)$$

The subscripts run as $I = 1, \dots, m$ and $A = +, \times, \circ, \ell, x, y$. The components are defined in Fourier space as $\hat{x}_I(f_j) := \tilde{x}_I(f_j)/\sqrt{S_n^I(f_j)}$, $\hat{F}_I^A(\hat{\Omega}, f_j) := F_I^A(\hat{\Omega})/\sqrt{S_n^I(f_j)}$, and $\hat{\eta}_I(f_j) := \tilde{\eta}_I(f_j)/\sqrt{S_n^I(f_j)}$, $j = 0, \dots, N-1$. $\tilde{x}(f_j)$ is defined as j -th component of the Fourier transform of $x(t)$:

$$\tilde{x}(f_j) := \sum_{k=0}^{N-1} x(j\Delta_t) \exp(-2\pi i k \Delta_t f_j). \quad (30)$$

N is the number of samplings, Δ_t is a sampling period, $\Delta_f := (N\Delta_t)^{-1}$ is a frequency resolution, and $f_j = j\Delta_f$. $\hat{x}_I(f_j)$, the whitened $\tilde{x}(f_j)$, is obtained by dividing by the power spectrum density $S_n^I(f_j)$ of I -th detector at a frequency f_j . There are several purposes to whiten detector data. The sensitivity of an interferometric GW detector is limited in a frequency-dependent way through a diverse noise budget [38]. Since multiple data streams have different transfer functions in the Fourier domain, one needs to whiten the data streams in order to combine them coherently. Otherwise insensitive frequency regions or insensitive detectors in a detector network dominate when the detection statistics is calculated. If data is whitened, these frequency regions or detectors are less-weighted naturally. Another important purpose of the data conditioning is to make the data un-correlated between samples by a whitening filter, and to mitigate the effect of instrumental artifacts in detector data. For instance, noise artifacts appear in multiple detectors with

the same frequency regions, can be correlated noise between detectors and this makes the detection efficiency reduced.

We first consider the reconstruction of waveforms in an ideal case without noise. In general, \mathbf{F} is not a squared matrix with full rank, hence we introduce the Moore-Penrose pseudo-inverse matrix \mathbf{M} as

$$\mathbf{M}\mathbf{h} = \mathbf{F}^T \mathbf{x}, \quad \text{where} \quad \mathbf{M} := \mathbf{F}^T \mathbf{F}. \quad (31)$$

If the detectors are not all co-aligned, \mathbf{M} is an invertible $A \times A$ matrix. Multiplying the equation by the inverse of \mathbf{M} , we get

$$\mathbf{h} = \mathbf{F}^\dagger \mathbf{x}, \quad \text{where} \quad \mathbf{F}^\dagger := \mathbf{M}^{-1} \mathbf{F}^T. \quad (32)$$

The inverse matrix \mathbf{M}^{-1} can be found from the formula

$$\mathbf{M}^{-1} = \frac{1}{\det(\mathbf{M})} \text{adj}(\mathbf{M}), \quad (33)$$

where $\text{adj}(\mathbf{M})$ is the adjoint matrix and $\det(\mathbf{M})$ is the determinant of \mathbf{M} . If (i, j) -th cofactor is defined as $C_{AA'} = [\text{adj}(\mathbf{M})]_{AA'}$, we finally obtain

$$\mathbf{h}_A = \mathbf{H}_A \cdot \mathbf{x}, \quad (34)$$

$$\mathbf{H}_A = \frac{1}{\det(\mathbf{M})} \sum_{A'} C_{AA'} \cdot \mathbf{F}_{A'} \quad (35)$$

As discussed in [24], the factor $\det(\mathbf{M})$ of this formula plays an important role in separating the polarization modes. If there is degeneracy in the antenna pattern functions of a detector network and $\det(\mathbf{M}) = 0$, we cannot reconstruct the polarization modes at all. Fortunately, this is not the case for current ground-based detectors.

We use a maximum likelihood method to estimate \mathbf{h} from the data. The maximum likelihood method maximizes

$$L[\mathbf{h}] := -\|\mathbf{x} - \mathbf{F}\mathbf{h}\|^2, \quad (36)$$

$$= -\|\mathbf{x} - \mathbf{F}\mathbf{F}^\dagger \mathbf{x}\|^2, \quad (37)$$

where $\|\cdot\|$ is defined by

$$\|\mathbf{x}\| := \left[\sum_{I=1}^m \sum_{j=0}^{N-1} |\hat{x}_I(j\Delta_f)|^2 \Delta_f \right]^{1/2}. \quad (38)$$

Introducing $\mathbf{Q} := \mathbf{I} - \mathbf{F}\mathbf{F}^\dagger$ and using \mathbf{Q} in Eq. (37), we obtain

$$L[\mathbf{h}] = -\|\mathbf{Q}\mathbf{x}\|^2, \quad (39)$$

We note $\mathbf{Q}\mathbf{F} = 0$, which means that \mathbf{Q} projects onto the null space of $\mathbf{F}\mathbf{F}^T$. From Eq. (39), one can see $L[\mathbf{h}]$ is equivalent to the null stream energy [39]. Suppose the

true source location is $\hat{\Omega}_s := (\phi_s, \theta_s)$,

$$\begin{aligned} L[\mathbf{h}] &= - \|\mathbf{Q}(\mathbf{F}(\hat{\Omega}_s)\mathbf{h} + \boldsymbol{\eta})\|^2 \\ &= - \|\mathbf{Q}\mathbf{F}(\hat{\Omega}_s)\mathbf{h}\|^2 - 2\text{Re} \left[\sum_j (\boldsymbol{\eta}^\dagger \mathbf{Q}\mathbf{F}(\hat{\Omega}_s)\mathbf{h})_j \Delta_f \right] \\ &\quad - \sum_j (\boldsymbol{\eta}^\dagger \mathbf{Q}\boldsymbol{\eta})_j \Delta_f. \end{aligned} \quad (40)$$

Here, we used the relation $\mathbf{Q}^2 = \mathbf{Q}$ and denoted frequency components as $(\boldsymbol{\eta}^\dagger \mathbf{Q}\boldsymbol{\eta})_j = [\boldsymbol{\eta}^\dagger \mathbf{Q}\boldsymbol{\eta}](f_j)$. As Ref. [35] shows, if we take the expectation value of the likelihood function in a stationary noise case, the first term in Eq. (40) is the same as the current value $\|\mathbf{Q}\mathbf{F}(\hat{\Omega}_s)\mathbf{h}\|^2$ and the second term vanishes. The third term at j -th frequency bin is

$$\begin{aligned} \langle (\boldsymbol{\eta}^\dagger \mathbf{Q}\boldsymbol{\eta})_j \rangle &= \sum_{I,J}^m Q_{IJ}^j \langle (\hat{\eta}_I^j)^* \hat{\eta}_J^j \rangle \\ &= \sigma_j^2 \sum_{I,J}^m \delta_{IJ} Q_{IJ}^j \\ &= \sigma_j^2 \text{tr}(\mathbf{Q}^j), \end{aligned} \quad (41)$$

where δ_{IJ} is Kronecker delta. Since the noise in the detectors is whitened, the noise can be regarded as the Gaussian white noise with its variance $\sigma^2 := \sum_j \sigma_j^2 \Delta_f$, where σ_j^2 is defined by $\langle (\hat{\eta}_I^j)^* \hat{\eta}_J^j \rangle = \delta_{IJ} \sigma_j^2$. We note σ_j^2 has the same value for all j -th frequency bin since the noise $\hat{\eta}$ is whitened. Transforming \mathbf{Q}^j to the diagonal form, we find $\text{tr}(\mathbf{Q}^j) = m - n$ and finally obtain

$$\langle L[\mathbf{h}] \rangle = - \|\mathbf{Q}\mathbf{F}(\hat{\Omega}_s)\mathbf{h}\|^2 - (m - n)\sigma^2, \quad (42)$$

where n is the total number of polarization modes. Since $\mathbf{Q}\mathbf{F}(\hat{\Omega}_s) = \mathbf{0}$ at the true location, $L[\mathbf{h}]$ become maximum.

We emphasize that the algorithm does not specify any alternative theories of gravity and can be applied to any number of polarization modes if it is less than the number of detectors. Therefore, this approach is a model-independent probe alternative theories of gravity.

III. APPLICATION TO THREE POLARIZATION MODES

A. Scalar GW in Brans-Dicke theory

There are several simulations on the spherically symmetric core collapse in the Brans-Dicke theory [11], which is a class of scalar-tensor theory. The scalar gravitational waveform is consistent with each simulation [40–45]. Therefore we use a waveform simulated by Shibata et al. [40]. In their simulation, they assumed the Brans-Dicke theory with the scalar field coupling to gravity, $\omega_{\text{BD}} = 50$ and 500, and calculated scalar gravitational

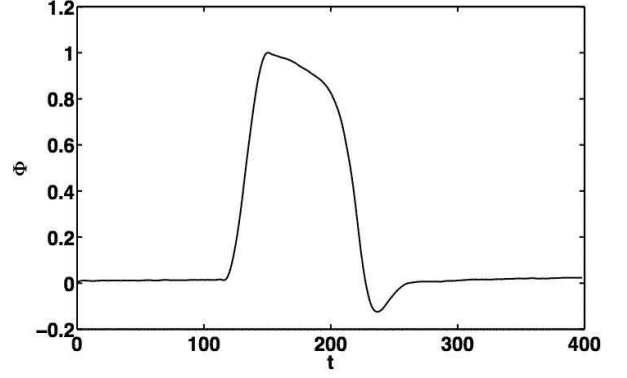


FIG. 2: A scalar gravitational waveform simulated by Shibata et al.[40] with the mass of the progenitor $10M_\odot$, $\omega_{\text{BD}} = 40000$, the distance from the earth 10Mpc . The unit of the time t is $4.93 \times 10^{-5}(M/10M_\odot)$. Φ is the normalized strain amplitude.

waveforms. They found the scalar fields are linearly scaled with ω_{BD} , and the scalar gravitational waveforms with different ω_{BD} are almost the same by scaling ω_{BD} . We therefore extrapolate the waveforms to larger values of ω_{BD} . The simulated scalar GW signal h is

$$h(t) = 1.25 \times 10^{-21} \left(\frac{M}{10M_\odot} \right) \left(\frac{10\text{kpc}}{R} \right) \left(\frac{40000}{\omega_{\text{BD}}} \right) \Phi(t) \quad (43)$$

where M is the mass of a progenitor, R is the distance from the earth. The shape of the waveform $\Phi(t)$ is in Figure 2. Since the unit of the time t in Figure 2 is $4.93 \times 10^{-5}(M/10M_\odot)$, The duration of the signal is linearly dependent of a mass of a progenitor.

B. Sensitivity to the scalar mode

Sensitivity of the designed Japanese interferometric GW detector KAGRA [46] to a scalar GW simulated by Shibata et al. [40] is estimated. We should note that more realistic estimation of the detectability needs more realistic simulation. However, we use Shibata's result for the purpose of demonstration. The top plot in Fig. 3 shows $h_{\text{rss}}-f_c$ of GWs from spherically symmetric core collapse supernovae located at 10kpc from the earth with $\omega_{\text{BD}} = 500, 1000, 2000, 4000, 8000, 16000, 40000, 80000, 160000$. h_{rss} is the root sum square of h defined as

$$h_{\text{rss}} := \left(\int_{-\infty}^{\infty} dt \sum_A h_A^2(t) \right)^{1/2}, \quad (44)$$

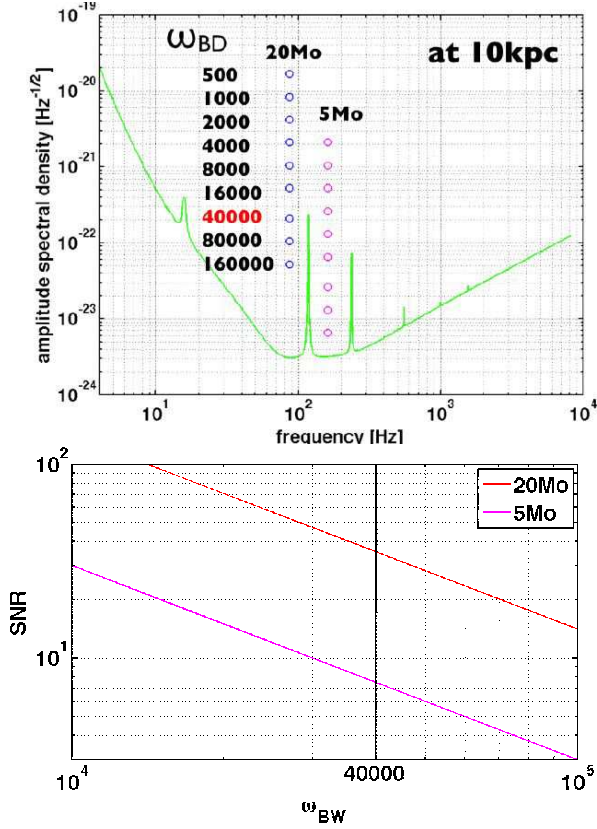


FIG. 3: Blue open circles are $h_{\text{rss}}-f_c$ of spherically symmetric core collapse supernovae at the distance 10kpc with the progenitor mass $20M_\odot$ and $\omega_{\text{BD}} = 500, 1000, 2000, 4000, 8000, 16000, 40000, 80000, 160000$. h_{rss}, f_c are defined in the text. Magenta open circles are for the progenitor mass $5M_\odot$. The bottom plot is $\omega_{\text{BD}}\text{-SNR}$. SNR is defined in the text. The red line is the one with the mass of the progenitor $20M_\odot$, the magenta line $5M_\odot$.

$A = +, \times, \circ$, and f_c is the characteristic frequency [47]

$$f_c := \left(\int_0^\infty \frac{\sum_A \tilde{h}_A(f) \tilde{h}_A^*(f)}{S_n(f)} f df \right) \times \quad (45)$$

$$\left(\int_0^\infty \frac{\sum_A \tilde{h}_A(f) \tilde{h}_A^*(f)}{S_n(f)} df \right)^{-1}, \quad (46)$$

where $\tilde{x}(f)$, $S_n(f)$, $\tilde{h}_A(f)$ are detector output, the noise power spectrum density, the plus, cross, and scalar modes of a GW in Fourier domain. \tilde{h}_A^* expresses its complex conjugate. Note that here we are considering GWs from spherically symmetric core collapse supernovae, which does not radiate tensor modes, namely, $h_+(t) = h_\times(t) = 0$. h_{rss} of the supernovae with the progenitor mass of $20M_\odot$ at the distance 10kpc are shown with blue open circles. The magenta open circles are the same except the mass of the progenitor is $5M_\odot$. These plots are on the current design sensitivity curve of KAGRA. The bottom plot in Fig. 3 shows estimated signal-to-noise ratio

(SNR) as a function of ω_{BD} . The SNR is defined as

$$\text{SNR} := \left(\int_{-\infty}^{\infty} \frac{\sum_A \tilde{x}(f) \tilde{h}_A^*(f)}{S_n(f)} df \right)^{1/2}. \quad (47)$$

We note that the SNR defined here is that of the matched filter method [48], which is the optimal case with respect to the antenna pattern function of the detector. The SNR is estimated by

$$\text{SNR} \simeq \frac{h_c}{\sqrt{f_c S_n(f_c)}}, \quad (48)$$

where h_c is the characteristic strain amplitude [47]

$$h_c := \left(3 \int_0^\infty \frac{S_n(f_c)}{S_n(f)} \sum_A \tilde{h}_A(f) \tilde{h}_A^*(f) f df \right)^{1/2}. \quad (49)$$

The red and magenta lines are the ones with the mass of the progenitor $20M_\odot$ and $5M_\odot$, respectively. The current upper limit on ω_{BD} is > 40000 by Cassini's observation in the solar system [49]. If a scalar GW with $\omega_{\text{BD}} = 40000$ is radiated from a spherically symmetric core collapse supernova at 10 kpc from the earth, KAGRA can detect the signal with SNR of 35 for the mass of $20M_\odot$ progenitor, 7 for the mass of $5M_\odot$ progenitor. In order to set upper limit on ω_{BD} , one has to know the distance of a source because the distance and ω_{BD} influence the amplitude of the GW at a detector in the same way. Therefore the two parameters are degenerated. It is important to combine usual astronomical observation such as electromagnetic observations and neutrino observations with the GW observation, so called the *multi-messenger observation*. Suppose it find a supernova occurs within our Galaxy through the multi-messenger observation. The above results indicates one may set stronger upper limit on ω_{BD} , or if the scalar GW is detected, one can determine ω_{BD} .

C. Reconstruction of three polarization modes

In the case the tensor and scalar modes exist, h_+ , h_\times , h_\circ are reconstructed as the linear combination of the antenna patterns of all the three polarizations. \mathbf{H}_A

($A = +, \times, \circ$) can be explicitly calculated from Eq. (35):

$$\begin{aligned} H_+ &= \frac{1}{\det(\mathbf{M})} [(\mathbf{F}_\times \times \mathbf{F}_\circ) \cdot (\mathbf{F}_\times \times \mathbf{F}_\circ) \mathbf{F}_+ \\ &\quad - (\mathbf{F}_\times \times \mathbf{F}_\circ) \cdot (\mathbf{F}_+ \times \mathbf{F}_\circ) \mathbf{F}_\times \\ &\quad + (\mathbf{F}_\times \times \mathbf{F}_\circ) \cdot (\mathbf{F}_+ \times \mathbf{F}_\times) \mathbf{F}_\circ], \end{aligned} \quad (50)$$

$$\begin{aligned} H_\times &= \frac{1}{\det(\mathbf{M})} [-(\mathbf{F}_+ \times \mathbf{F}_\circ) \cdot (\mathbf{F}_\times \times \mathbf{F}_\circ) \mathbf{F}_+ \\ &\quad + (\mathbf{F}_+ \times \mathbf{F}_\circ) \cdot (\mathbf{F}_+ \times \mathbf{F}_\circ) \mathbf{F}_\times \\ &\quad - (\mathbf{F}_+ \times \mathbf{F}_\circ) \cdot (\mathbf{F}_+ \times \mathbf{F}_\times) \mathbf{F}_\circ], \end{aligned} \quad (51)$$

$$\begin{aligned} H_\circ &= \frac{1}{\det(\mathbf{M})} [(\mathbf{F}_+ \times \mathbf{F}_\times) \cdot (\mathbf{F}_\times \times \mathbf{F}_\circ) \mathbf{F}_+ \\ &\quad - (\mathbf{F}_+ \times \mathbf{F}_\times) \cdot (\mathbf{F}_+ \times \mathbf{F}_\circ) \mathbf{F}_\times \\ &\quad + (\mathbf{F}_+ \times \mathbf{F}_\times) \cdot (\mathbf{F}_+ \times \mathbf{F}_\times) \mathbf{F}_\circ]. \end{aligned} \quad (52)$$

The symbols \times and \cdot denote the outer product and the inner product, respectively. We note if $\det(\mathbf{M}) = 0$, which happens when detectors are co-aligned, the reconstruction of any polarization mode fails. However, this is not the case for the current ground-based detector network.

IV. SIMULATION OF RECONSTRUCTION OF POLARIZATION MODES

A. Implementation

For the data conditioning, the linear predictor error filter is used, assuming data is a stationary stochastic process and can be expressed by an autoregressive model with order of P . If predicted data stream can be written as

$$x'(s\Delta_t) = \sum_{p=1}^P c(p\Delta_t)x((s-p)\Delta_t), \quad (53)$$

the linear predictor error filter finds parameters $c(p\Delta_t)$ which minimize the prediction error

$$x_w(s\Delta_t) := x(s\Delta_t) - x'(s\Delta_t) \quad (54)$$

$$:= \sum_{p=0}^P b(p\Delta_t)x((s-p)\Delta_t) \quad (55)$$

using Yule-Walker method [50]. Here $b(p\Delta_t) := \delta_{p0} - c(p\Delta_t)$, $c(0) := 0$. This filter has a group delay of the phase especially near narrowband spectral feature and the timing error between the whitened data of different detectors is introduced. To cancel the timing error, the linear predictor filter is first applied causally and then anti-causally,

$$\tilde{x}_w(f) = \tilde{B}(f)\tilde{B}^*(f)\tilde{x}(f), \quad (56)$$

where $\tilde{x}_w(f)$ is the discrete time Fourier transform of whitened data,

$$\tilde{B}(f) := \sum_{m=0}^{\infty} b(p\Delta_t) \exp(-i2\pi fp/f_s), \quad (57)$$

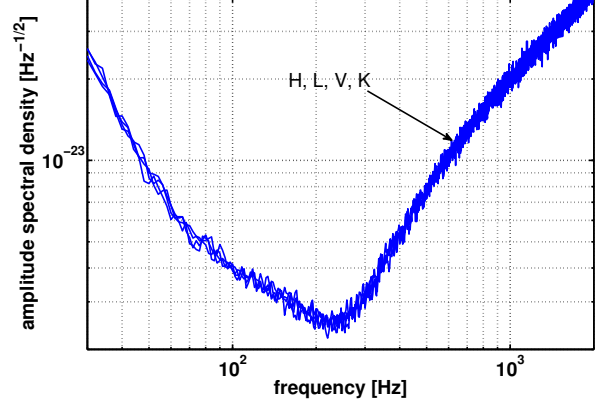


FIG. 4: The sensitivity curves. The x -axis is frequency and the y -axis is amplitude spectrum density. Detectors considered are H, L, V, K with the same sensitivity which is similar to the design sensitivity of advanced LIGO.

f_s is a sampling frequency of the data [51]. The filter coefficients $b(p\Delta_t)$ is estimated using a stationary data segment. For this purpose, we use a few seconds data segment that does not have non-stationary noise in the implementation. The data segment will not be used for search for GWs. We then construct the finite impulse response (FIR) filter with the coefficients $b(p\Delta_t)$ and pass the data through the FIR filter to whiten it.

Set of the whitened data \mathbf{x} of the multiple detectors with equal length is passed to the coherent network analysis pipeline. The value of the likelihood of the data which is maximized over all possible h_+ , h_\times , and h_\circ with durations less than or equal to the data length. The likelihood values are obtained as a function of θ and ϕ . This two-dimensional output, $\mathcal{S}(\theta, \phi)$, is called *skymap*. Finally reconstructed h_+ , h_\times and h_\circ are evaluated the maximum point of the skymap. We note that the implementation is based on the paper [36].

B. Reconstruction of the polarization modes without tensor mode signals

We perform Monte Carlo simulations to reconstruct the scalar polarization of a GW. The network consisted of the 4 km LIGO Hanford (H), LIGO Livingston (L), VIRGO (V), and KAGRA (K) interferometers [6–8]. For the detector noise amplitude spectral densities, we use the design sensitivity curves similar to the advanced LIGO detectors as given in [52] (see Fig. 4) and keep the locations and orientations the same as the real detectors. The stationary noise is generated 50 seconds by first using 4 independent realizations of Gaussian white noise and then passing them through FIR filters having transfer functions that *approximately* match the design curves. The generated data is sampled at 16384 Hz and

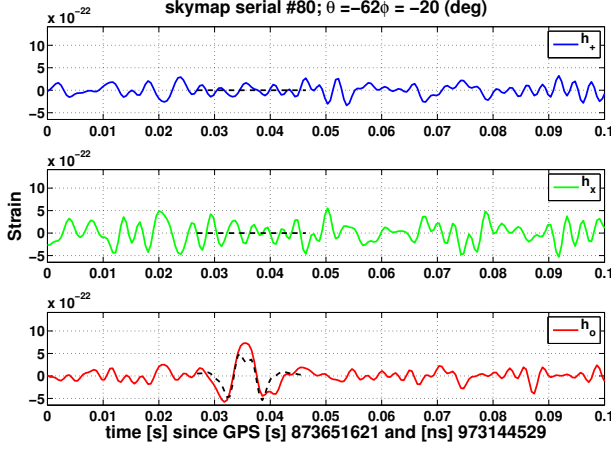


FIG. 5: Reconstructed polarization modes. The top plot is h_+ , the middle plot is h_\times , the bottom plot is h_o . The x axis is time with the unit of millisecond since GPS time 873651621.97314453[s]. The black dashed line in each plot is the injected signal.

then passed through the data conditioning pipeline. Besides downsampling the data to 2048 Hz by applying the same anti-aliasing filter to all data streams, the data conditioning pipeline applies time domain whitening filters that are trained on the first five seconds of data in which any injected signal is not included. In this simulation we put cut-off frequencies at 60 Hz and 400 Hz so that lower and higher frequencies are filtered.

We assume that the GW source is a spherically symmetric core collapse supernovae. The injected signals corresponds to a single source located at the right ascension (RA) of 15 hours and the declination (DEC) of -60 degrees. The mass of the progenitor is $10M_\odot$, $\omega_{BD} = 40000$, the distance from the earth is 10kpc. we here assume that $h_\times(t)$ and $h_+(t)$ are absent and that the simulated gravitational waveform is h_o . In the next subsection, we will perform the same simulation in the presence of $h_\times(t)$ and $h_+(t)$.

Fig. 5 shows the reconstruction of h_+ , h_\times , h_o , which is one of segments triggered by the pipeline. In the reconstructed time-series of h_o , the injected signal is clearly reconstructed. The injected h_o different from Figure 2. This difference comes from the fact that the low frequency region below 60 Hz and the high frequency region above 400 Hz in data are filtered in this simulation.

In this paper, it is supposed that the gravitational waveform is known and the matched filter method is applicable to the search. To evaluate the accuracy of the reconstruction, the SNR is calculated in the same way of Eq. (47):

$$\text{SNR} = \left(\int_{-\infty}^{\infty} \frac{\sum_A \tilde{h}_A(f) \tilde{h}_A^*(f)}{S_{nA}(f)} df \right)^{1/2}, \quad (58)$$

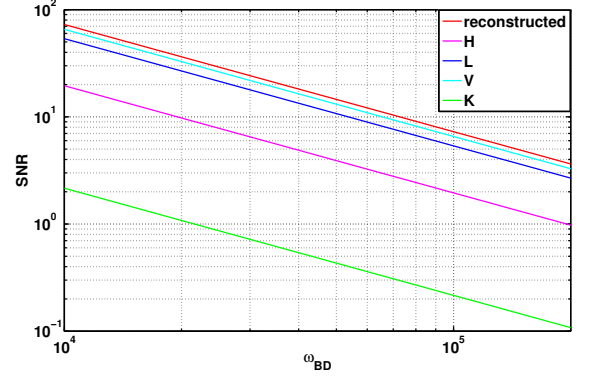


FIG. 6: The SNR of $F_o h_o$ in H, L, V, and K, and reconstructed h_o as a function of ω_{BD} .

where $\tilde{h}_A(f)$ is the reconstructed h_A in Fourier domain, $\tilde{h}_A(f)$ is the injected h_A in Fourier domain, and $S_{nA}(f)$ is the power spectrum density of the reconstructed h_A . It should be noted that realistic searches for GWs from supernovae cannot use the waveform models because the models are still not well-established at present. The realistic search may use other indicators which do not use waveform models such as the excess power statistics [53].

The SNR of the reconstructed h_o which is band-filtered is 14.3. The SNR of h_o in H, L, V, K before the reconstruction is 4.9, 13.4, 16.4, 0.54. F_o is -0.26 for H, 0.42 for L, -0.45 for V, -0.01 for K. The main contribution to the SNR is from V which has best antenna pattern among them.

Fig. 6 shows the SNR of h_o in H (the magenta line), L (the blue line), V (the light blue line), and K (the green line), and reconstructed h_o (the red line) as a function of ω_{BD} . The reconstruction procedure were repeated 28 times with different data set and the SNRs were calculated at each trial and then they were averaged. Interestingly, the SNR of the reconstructed h_o is higher than the others. As shown in Eq. (37), the maximum likelihood method combines all detector data streams that are weighted by their sensitivities in the whitening procedure. Multiple sensitive-detector data streams make contribution to reduce the variance of the reconstructed h_o and the SNR of the reconstructed h_o rises up. In regard to constraining ω_{BD} by practical GW observations, further studies including the difference of each detector sensitivity and the dependence of SNR on a sky position are needed.

C. Reconstruction of the polarization modes with tensor mode signals

In previous section we considered the reconstruction of the GW which contains only scalar mode. The algorithm can reconstruct all the modes if they exist. In

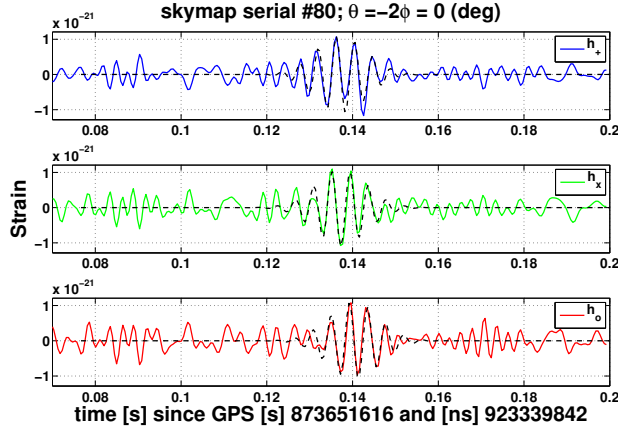


FIG. 7: Reconstructed h_+ , h_\times , and h_o . The black dashed line on each plot is the injected waveform.

in this section we demonstrate the reconstruction of a GW which contains three modes, h_+ , h_\times , h_o . Example of the reconstruction of the polarization modes h_+ , h_\times , and h_o is shown in Fig. 7. The detectors H, L, V, K are assumed to have the same sensitivity as shown in Fig. 4. The set of detector noise is generated in the same way as in section IV. Regarding to injection signals, in this simulation we will not use GW waveforms predicted by the Brans-Dicke theory because spherically symmetric core collapse supernovae do not produce tensor modes, and there is no realistic simulations on asymmetric core collapses in the Brans-Dicke theory. Instead, we will use the sine-Gaussian signals that are usually used for evaluation of GW burst searches. The injected signals correspond to a single source located at the right ascension (RA) of 16.4 hours and the declination (DEC) of 0 degrees. We assume that

$$h_\times(t) = A \exp[-(2\pi f_0 t)^2 / 2Q^2] \sin(2\pi f_0 t), \quad (59)$$

$$h_+(t) = A \exp[-(2\pi f_0 t)^2 / 2Q^2] \sin(2\pi f_0 t + \pi/2), \quad (60)$$

$$h_o(t) = A \exp[-(2\pi f_0 t)^2 / 2Q^2] \sin[2\pi f_0 (t + 0.003)], \quad (61)$$

where $Q = 9$ is the Q -value and $f_0 = 235$ Hz is the central frequency. The signal strength A is scaled so that the root-sum-square $h_{\text{rss}} = 1.38 \times 10^{-22} \text{ Hz}^{-1/2}$. The dashed lines in Fig. 7 are the injection signals. We evaluate the signal strength by SNR. Table I shows the SNR of the reconstructed h_+ , h_\times , h_o , and the SNR before reconstruction of the three polarization modes in H, L, V, K.

If we define a mean SNR as

$$\overline{\text{SNR}} = \sqrt{\frac{\text{SNR}(h_+)^2 + \text{SNR}(h_\times)^2 + \text{SNR}(h_o)^2}{3}}, \quad (62)$$

$\overline{\text{SNR}}$ is 20.1 for reconstructed modes, 12.7 for H, 16.7 for L, 18.7 for V, 15.9 for K. From the Table I, one can see

	Reconstructed	H	L	V	K
h_+	23.3	8.3	9.6	26.7	24.5
h_\times	20.2	15.4	18.0	15.4	10.8
h_o	16.3	13.3	20.4	10.0	6.2

TABLE I: The SNR of the reconstructed h_+ , h_\times , h_o , and the SNR of the three polarization modes in H, L, V, K. The antenna pattern function (F_+ , F_\times , F_o) is (0.25, -0.46, 0.39) for H, (0.19, 0.36, -0.41) for L, (-0.65, -0.38, -0.24) for V, (0.56, 0.25, 0.14) for K.

even if several detectors in the detector network do not have sensitivities to certain polarization modes, sensitive detectors in the detector network can make improvement of the SNR. One indication to know the detector-network sensitivity to the polarization modes is the network antenna pattern skymap $\bar{F}_T := \sqrt{(\sum_{I=1}^m F_+^{I2} + F_\times^{I2})}$, $\bar{F}_S := \sqrt{(\sum_{I=1}^m F_o^{I2})}$, $\bar{F}_V := \sqrt{(\sum_{I=1}^m F_x^{I2} + F_y^{I2})}$. Figure 8 shows the network antenna pattern skymap of H-L-V-K. Comparing the antenna pattern skymaps of the polarization modes for H (see Figure 1), for the antenna pattern skymaps of the tensor modes, the region where the value is above 0.5 is increased from 72.8% to 100%, for the vector modes, the region where the value is above 0.5 is increased from 69.1% to 100%, and for the scalar mode, the region where the value is above 0.25 is increased from 31.4% to 94.2%. These shows the benefit of the use of multiple detectors in terms of the improvement of the SNR and the sky coverage. The latter means that angular directions insensitive to a certain polarization mode is removed and that the detector network can distinguish all polarizations. It should be noted that the matched filtering method on reconstructed polarization modes is proposed in [54]. This method benefit from the detector network directly.

V. SUMMARY

This paper proposed a method to reconstruct at most five non-Einsteinian polarization modes, in addition to h_+ and h_\times , of GWs using a network of ground-based interferometric GW detectors. This method is applicable for testing alternative theories of gravity by searching for scalar and vector GWs. Since the method does not rely on any specific model of the proposed alternative theories and does not need theoretical models of gravitational waveforms, the method can be a model-independent test of alternative theory of gravity.

We overview the algorithm of the method. The detector responses is first whitened by the linear predictor error filter so that the processed data is sample to sample uncorrelated. Since the detector response to a GW is the linear combination of the polarization modes weighted with the antenna pattern functions, the reconstruction of the polarization modes is naturally formulated as an inverse problem. We solved the inverse problem by min-

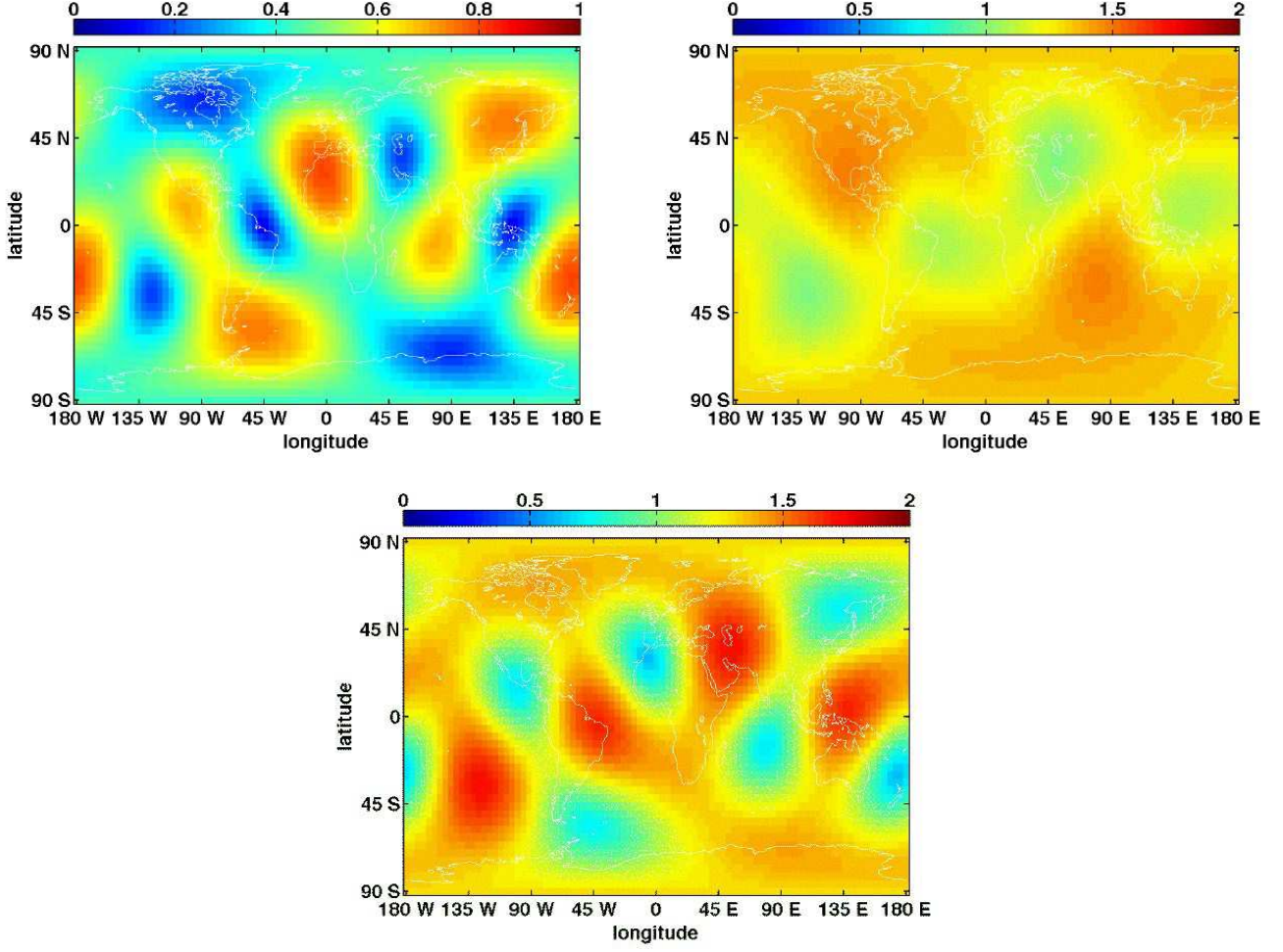


FIG. 8: The left top plot is the network antenna pattern of H-L-V-K to a scalar gravitational wave. The X-axis is the longitude and the Y-axis is the latitude. The right top plot is the network antenna pattern function to the tensorial modes. The bottom plot is the summed antenna pattern function to the vector modes

imizing residuals by subtracting a reconstructed signal from the detector output data.

We performed simulations of the reconstruction of the polarization modes as demonstrations. We used the simulated gravitational waveform from a spherically symmetric core collapse supernova in Brans-Dicke theory, which predicts only the scalar GW, and showed the scalar GW was well reconstructed. We also demonstrated that all gravitational waveforms were well reconstructed in the presence of two tensor modes in addition to a scalar mode, using sine-Gaussian waveforms. The mean SNR defined in Eq. (62) was calculated for the reconstructed polarization modes and the polarization modes in H, L, V, K before reconstruction. The mean SNR of the reconstructed polarizations were higher than the others, which means that sensitive detectors play an important role to reconstruct the waveforms and gain the SNR. For further study of the detectability, more realistic simulations, considering the sky position dependence of a source and

other waveforms in a specific model of gravity theory, are encouraged.

Finally we discuss the case that other polarization modes than the three polarization modes exist. In this case, because \mathbf{Q} does not project onto the null space of $\mathbf{F}\mathbf{F}^T$ where \mathbf{F} includes all polarization modes, $L[\mathbf{h}]$ has larger variance than expected noise variance in Eq. (42) even if (θ, ϕ) is the true source location. Therefore we can test the existence of other polarization modes.

Acknowledgments

K.H. is supported by Grant-in-Aid for Young Scientists (B) and the Max-Planck-Society. K.H. would like to thank to Bruce Allen for warm hospitality during his stay in Hannover. K.H. would like to thank to Soumya D. Mohanty for valuable comments and encouragement. A.N. is supported by a grant-in-aid through JSPS. We

would like to thank to Atsushi Taruya for fruitful discussion.

-
- [1] The LIGO Scientific Collaboration and The Virgo Collaboration, *Nature* **460**, 990 (2009).
 - [2] J. Abadie et al., *Phys. Rev. D* **85**, 102001 (2010).
 - [3] B. P. Abbott et al., *Astrophys. J.* **713**, 671 (2010).
 - [4] B. P. Abbott et al., *Phys. Rev. D* **80**, 102002 (2009).
 - [5] B. P. Abbott et al., *Phys. Rev. D* **80**, 102001 (2009).
 - [6] Advanced LIGO webpage, <http://www.ligo.caltech.edu/advLIGO/scripts/summary.shtml>, <http://www.ligo.caltech.edu/ligo2/>.
 - [7] Advanced VIRGO webpage, <http://wwwcascina.virgo.infn.it/advirgo/>.
 - [8] KAGRA webpage, <http://gwcenter.icrr.u-tokyo.ac.jp/en/>.
 - [9] D. M. Eardley, D. L. Lee, A. P. Lightman, R. V. Wagoner, and C. M. Will, *Phys. Rev. Lett.* **30**, 884 (1973).
 - [10] C. M. Will, *Theory and experiment in gravitational physics*, (Cambridge University Press (1993)).
 - [11] C. Brans and R. H. Dicke, *Phys. Rev.* **124**, 925 (1961).
 - [12] Y. Fujii and K. Maeda, *The Scalar-Tensor Theory of Gravitation*, (Cambridge University Press (2002)).
 - [13] T. P. Sotiriou and V. Faraoni, arXiv:0805.1726.
 - [14] A. de Felice and S. Tsujikawa, *Living Rev. Rel.* **13**, 3 (2010).
 - [15] M. E. S. Alves, O. D. Miranda, and J. C. N. de Araujo, *Phys. Lett. B* **679**, 401 (2009).
 - [16] M. E. S. Alves, O. D. Miranda, and J. C. N. de Araujo, *Class. Quantum Grav.* **27**, 145010 (2010).
 - [17] M. Visser, *Gen. Relativ. Gravit.* **30**, 1717 (1998).
 - [18] V. A. Rubakov and P. G. Tinyakov, *Physics Uspekhi* **51**, 759 (2008).
 - [19] C. de Rham, G. Gabadadze, and A. J. Tolley, *Phys. Rev. Lett.* **106**, 231101 (2011).
 - [20] C. de Rham, G. Gabadadze, and A. J. Tolley, *J. High Energy Phys.* **11**, 093 (2011).
 - [21] C. M. Will, *Living Rev. Relativity* **9**, 3 (2006).
 - [22] K. J. Lee, F. A. Jenet, and R. H. Price, *Astrophys. J.* **685**, 1304 (2008).
 - [23] A. Nishizawa, A. Taruya, K. Hayama, S. Kawamura, and M.-A. Sakagami, *Phys. Rev. D* **79**, 082002 (2009).
 - [24] A. Nishizawa, A. Taruya, and S. Kawamura, *Phys. Rev. D* **81**, 104043 (2010).
 - [25] IndIGO webpage, <http://www.gw-indigo.org/tiki-index.php>.
 - [26] M. Maggiore and A. Nicolis, *Phys. Rev. D* **62**, 024004 (2000).
 - [27] M. E. Tobar, T. Suzuki, and K. Kuroda, *Phys. Rev. D* **59**, 102002 (1999).
 - [28] M. Tinto and M. E. S. Alves, *Phys. Rev. D* **82**, 122003 (2010).
 - [29] A. Blaut, *Phys. Rev. D* **85**, 043005 (2012).
 - [30] M. E. S. Alves and M. Tinto, *Phys. Rev. D* **83**, 123529 (2011).
 - [31] S. J. Chamberlin and X. Siemens, *Phys. Rev. D* **85**, 082001 (2012).
 - [32] Y. Gürsel and M. Tinto, *Phys. Rev. D* **40**, 3884 (1989).
 - [33] S. Klimentenko, S. Mohanty, M. Rakhmanov, and G. Mitselmakher, *Phys. Rev. D* **72**, 122002 (2005).
 - [34] S. D. Mohanty, M. Rakhmanov, S. Klimentenko, and G. Mitselmakher, *Classical and Quantum Gravity* **23**, 4799 (2006).
 - [35] M. Rakhmanov, *Class. Quantum Grav.* **23**, 673 (2006).
 - [36] K. Hayama, S. D. Mohanty, M. Rakhmanov, and S. Desai, *Classical and Quantum Gravity* **24**, 681 (2007).
 - [37] P. J. Sutton, G. Jones, S. Chatterji, P. Kalmus, I. Leonor, S. Poprocki, J. Rollins, A. Searle, L. Stein, M. Tinto, et al., *New Journal of Physics* **12**, 053034 (2010).
 - [38] A. Lazzarini and et al., LIGO technical document (1996).
 - [39] S. Chatterji, A. Lazzarini, L. Stein, P. J. Sutton, A. Searle, and M. Tinto, *Phys. Rev. D* **74**, 082005 (2006).
 - [40] M. Shibata, K. Nakao, and T. Nakamura, *Phys. Rev. D* **50**, 7304 (1994).
 - [41] M. Saijo, H.-a. Shinkai, and K.-i. Maeda, *Phys. Rev. D* **56**, 785 (1997).
 - [42] T. Harada, T. Chiba, K.-I. Nakao, and T. Nakamura, *Phys. Rev. D* **55**, 2024 (1997).
 - [43] T. Harada, *Phys. Rev. D* **57**, 4802 (1998).
 - [44] J. Novak, *Phys. Rev. D* **57**, 4789 (1998).
 - [45] J. Novak and J. M. Ibáñez, *Astrophys. J.* **533**, 392 (2000).
 - [46] <http://gwcenter.icrr.u-tokyo.ac.jp/en/researcher/parameter>.
 - [47] K. Thorne, in *Three Hundred Years of Gravitation*, edited by S. Hawking and W. Israel (Cambridge University Press, 1987), pp. 330–458.
 - [48] L. S. Finn, *Phys. Rev. D* **46**, 5236 (1992).
 - [49] B. Bertotti, L. Iess, and P. Tortora, *Nature* **425**, 374 (2003).
 - [50] J. Makhoul, *Proc. IEEE* **63** (1975).
 - [51] S. Chatterji, L. Blackburn, G. Martin, and E. Katsavounidis, *Class. Quantum Grav.* **21**, S1809 (2004).
 - [52] B. S. Sathyaprakash and B. F. Schutz, *Living Reviews in Relativity* **12**, 2 (2009).
 - [53] W. G. Anderson, P. R. Brady, J. D. Creighton, and É. É. Flanagan, *Phys. Rev. D* **63**, 042003 (2001).
 - [54] K. Hayama, S. D. Mohanty, S. Desai, M. Rakhmanov, T. Summerscales, and S. Yoshida, *Classical and Quantum Gravity* **25**, 184021 (2008).